How to cite: *Angew. Chem. Int. Ed.* **2023,** *62,* e202218044
International Edition: doi.org/10.1002/anie.202218044
German Edition: doi.org/10.1002/ange.202218044

Li Metal Batteries

Interface Design Enabling Stable Polymer/Thiophosphate Electrolyte Separators for Dendrite-Free Lithium Metal Batteries

Hanyu Huo, Ming Jiang, Boris Mogwitz, Joachim Sann, Yuriy Yusim, Tong-Tong Zuo, Yannik Moryson, Philip Minnmann, Felix H. Richter, Chandra Veer Singh,* and Jürgen Janek**

Abstract: Organic/inorganic interfaces greatly affect Li^+ transport in composite solid electrolytes (SEs), while SE/electrode interfacial stability plays a critical role in the cycling performance of solid-state batteries (SSBs). However, incomplete understanding of interfacial (in)stability hinders the practical application of composite SEs in SSBs. Herein, chemical degradation between Li_6PS_5Cl (LPSCl) and poly(ethylene glycol) (PEG) is revealed. The high polarity of PEG changes the electronic state and structural bonding of the PS_4^{3-} tetrahedra, thus triggering a series of side reactions. A substituted terminal group of PEG not only stabilizes the inner interfaces but also extends the electrochemical window of the composite SE. Moreover, a LiF-rich layer can effectively prevent side reactions at the Li/SE interface. The results provide insights into the chemical stability of polymer/sulfide composites and demonstrate an interface design to achieve dendrite-free lithium metal batteries.

Introduction

Since the commercialization of lithium-ion batteries (LIBs) in 1991, rechargeable devices make our daily life convenient.[1] However, current state-of-the-art LIBs cannot meet the increasing demands for high energy density, long cycle life, and fast charge. The rapidly rising market of electric vehicles also requires sufficient safety of large LIB packs for practical applications.[2] Unfortunately, the safety issue is an intrinsic bottleneck of LIBs due to the use of flammable liquid electrolytes. Under these circumstances, more attention focuses on solid-state batteries (SSBs), in which the flammable liquid electrolyte is replaced by solid electrolytes (SEs) to enhance battery safety.[3] In addition, SEs combined with high-voltage cathodes and a lithium metal anode are expected to achieve SSBs with high energy density.

It is generally acknowledged that interfacial stability plays a critical role in the electrochemical performance of SSBs.[4] Although thiophosphate SEs exhibit the highest lithium-ion conductivities of SEs, both their Li/SE and SE/cathode interfaces are unstable.[5,6] Degradation reactions between thiophosphate SEs and lithium metal lead to the formation of interfacial passivation layers, which not only can hinder Li^+ transport but also may induce lithium dendrite nucleation at the interface.[7] Due to the accumulated stress and inhomogeneous distribution of the electric field, the deteriorated interface during repeated cycling promotes the formation of cracks inside the thiophosphate SE. These cracks serve as pathways for lithium dendrite propagation until short-circuit of the SSB occurs.[8] In addition, the instability between thiophosphate SEs and cathode active materials (CAMs) is detrimental to the ion/electron transport in composite cathodes.[9] The introduction of conductive carbon can further accelerate the cathode/SE interfacial reactions, thus leading to low specific capacity and fast capacity decay.[10] Various characterization methods were employed to evaluate the degradation process, including X-ray photoelectron spectroscopy (XPS),[11] X-ray

[*] H. Huo, B. Mogwitz, J. Sann, Y. Yusim, T.-T. Zuo, Y. Moryson, P. Minnmann, F. H. Richter, J. Janek
Institute of Physical Chemistry, Justus Liebig University Giessen
Heinrich-Buff-Ring 17, 35392 Giessen (Germany)
and
Center for Materials Research (ZfM), Justus Liebig University Giessen
Heinrich-Buff-Ring 16, 35392 Giessen (Germany)
E-mail: Hanyu.Huo@phys.chemie.uni-giessen.de
Juergen.Janek@phys.chemie.uni-giessen.de
M. Jiang
Institute of Physical Science and Information Technology, Anhui University
Hefei, 230601 (China)
C. Veer Singh
Department of Materials Science and Engineering, University of Toronto
Toronto, Ontario, M5S 3E4 (Canada)
E-mail: chandraveer.singh@utoronto.ca

absorption near-edge spectroscopy (XANES),[12] and secondary-ion mass spectrometry (SIMS).[13]

Numerous strategies were employed to address the SE/electrode interfacial issues, such as artificial solid electrolyte interphases (SEI) of lithium anodes,[14] and coating layers of cathode particles.[15] However, the interfacial properties of the SE itself are usually ignored, which affects the quality of fabricated SEs. For inorganic SEs, large grain boundaries as internal interfaces reduce the effective ionic conductivity and can cause accumulation of electrons for direct Li^+ reduction in SEs.[16] Therefore, densification at high temperature or/and high pressure is applied during the fabrication of SEs to eliminate pores and anneal grain boundaries. Against this background, organic/inorganic composite SEs receive increasing attention due to expected thin separator thickness for high energy density and improved flexibility for large-scale production.[17]

In recent studies, poly(ethylene oxide) (PEO) polymer was mixed with various thiophosphate SE fillers, such as Li_6PS_5Cl (LPSCl),[18] $Li_7P_3S_{11}$ (LPS),[19] and $Li_{10}GeP_2S_{12}$ (LGPS)[20] to fabricate thin composite SE separators, yet little attention was paid to the interfacial stability between the polymer matrix and SE fillers. Considering that the PS_4^{3-} tetrahedral anion is sensitive to moisture and polar solvents, polar PEO may degrade sulfide SEs. The resulting instability at internal interfaces hinders Li^+ transport, thus leading to low effective ionic conductivity and increasing the risk of lithium dendrite growth. Moreover, to achieve the energy density goal of 350 $Wh\,kg^{-1}$, the thickness of hybrid electrolyte separators should be less than 60 μm.[21] Thin composite SEs show a lower shear modulus and shorter piercing distance for lithium dendrite growth compared to thick ceramic pellet SEs.[22] The narrow oxidation window of the PEO phase leads to strong degradation with high-voltage CAMs. Therefore, understanding interfacial stability and rational design of both stable internal and SE/electrode interfaces are significant for achieving SSBs with competitive performance.

Herein, we aim to understand the interfacial stability of SSBs based on thin polymer/thiophosphate composite SEs and rationally design the interfaces to advance dendrite-free lithium metal batteries. The chemical degradation between LPSCl and poly(ethylene glycol) (PEG) is revealed by several characterization methods and by density functional theory (DFT) simulations. In addition, we show that—compared to PEG—polyethylene glycol dimethyl ether (PEGDME) exhibits higher stability with LPSCl and an extended electrochemical window at high voltage due to the substituted terminal groups. The addition of LiFSI to the mixed lithium conducting salt forms a LiF-rich protection layer in contact with lithium metal. Although the LiFSI-induced SEI was reported previously,[23] the reaction mechanism and evolution of ion transport is unclear. In situ XPS and time-dependent electrochemical impedance spectroscopy (EIS) in this work help to better understand the SEI components and interface evolution. The best ionic conductivity of the composite SE is achieved with 15 wt % of PEGDME. The composite SEs with a thickness of 60 μm show homogeneous lithium plating/stripping with higher Coulomb efficiency (CE) than pristine LPSCl pellets with a thickness of 580 μm. High capacity retention of Li/$LiNi_{0.85}Co_{0.1}Mn_{0.05}O_2$ batteries is also observed under a relatively low stack pressure. Finally, we demonstrate the general applicability of our concept by forming analogous composite SEs with Cl-rich LPSCl and LGPS.

Results and Discussion

Chemical degradation between LPSCl and PEG

To evaluate the chemical stability between LPSCl and PEG, LPSCl powder was mixed with PEG (weight ratio = 8.5:1.5) in a mortar and heated at 100 °C for 24 h. The XRD pattern in Figure S1a shows that the used LPSCl powder exhibits a pure cubic argyrodite-type structure. Most LPSCl particles have a particle size of less than 5 μm, while a few particles with a size around 10 μm are also present (Figure S1b). The EIS analysis of a cold-pressed LPSCl pellet shows a lithium ionic conductivity of $\sigma_{ion} = 1.0 \times 10^{-3}$ $S\,cm^{-1}$ at 25 °C (Figure S1c). The used PEG shows the same molecular structure, but smaller molecular weight compared to PEO, while PEGDME shows the same polymer backbone (i.e. $-(O-CH_2-CH_2)_n-$) but substituted $-OCH_3$ terminal groups compared to PEG. The corresponding molecular structures are shown in Figure S2. Both PEG and PEGDME are solid at room temperature and liquid above 60 °C as demonstrated in light optical images in Figure S3. The molten PEG facilitates the thorough mixing with LPSCl particles, thus avoiding any influence from using solvents. The mixture of LPSCl and PEG was cooled to room temperature followed by XPS and Fourier-transform infrared spectroscopy (FT-IR) measurements.

Figures 1a and b show the S 2p and P 2p XPS spectra for the PEG/LPSCl composite, respectively. Several double peaks are obtained. The strong double peaks at 161.7 eV in the S 2p spectrum and 131.8 eV in the P 2p spectrum originate from the PS_4^{3-} tetrahedra of the argyrodite LPSCl structure (P–S–Li bonds).[13] The doublet at 160.1 eV in the S 2p spectrum corresponds to "free" S^{2-} ions in LPSCl.[24] We assume the third double peak at around 163.0 eV in the S 2p spectrum stems from the formation of polysulfides ($-S_x^0-$) or components with polysulfide bonds (P–$[S]_n$–P).[9,25] In addition, the peaks of species with P–O bonds (PS_xO_y) and reduced phosphorus species (P_{red}) are obtained in the P 2p spectrum, indicating the chemical decomposition of LPSCl.[26] The formation of polysulfides and reduced phosphorus are related to the high polarity of PEG, which facilitates the coordination of Li^+ from the LPSCl by PEG polymer chains.[27] The extraction of Li^+ leads to polymerization reactions of PS_4^{3-} units, thus forming oligomers such as $P_2S_8^{4-}$ and $P_2S_7^{4-}$.[28] The presence of these dissolved thiophosphates in the PEG explains the color change of the PEO/LGPS composite SE, which was observed by Gasteiger and co-workers after storing it in the glovebox for 3 months.[29] The decomposition of LPSCl goes hand in hand with the degradation of PEG by intramolecular reduction and bonding association of PEG with LPSCl. FT-IR shows

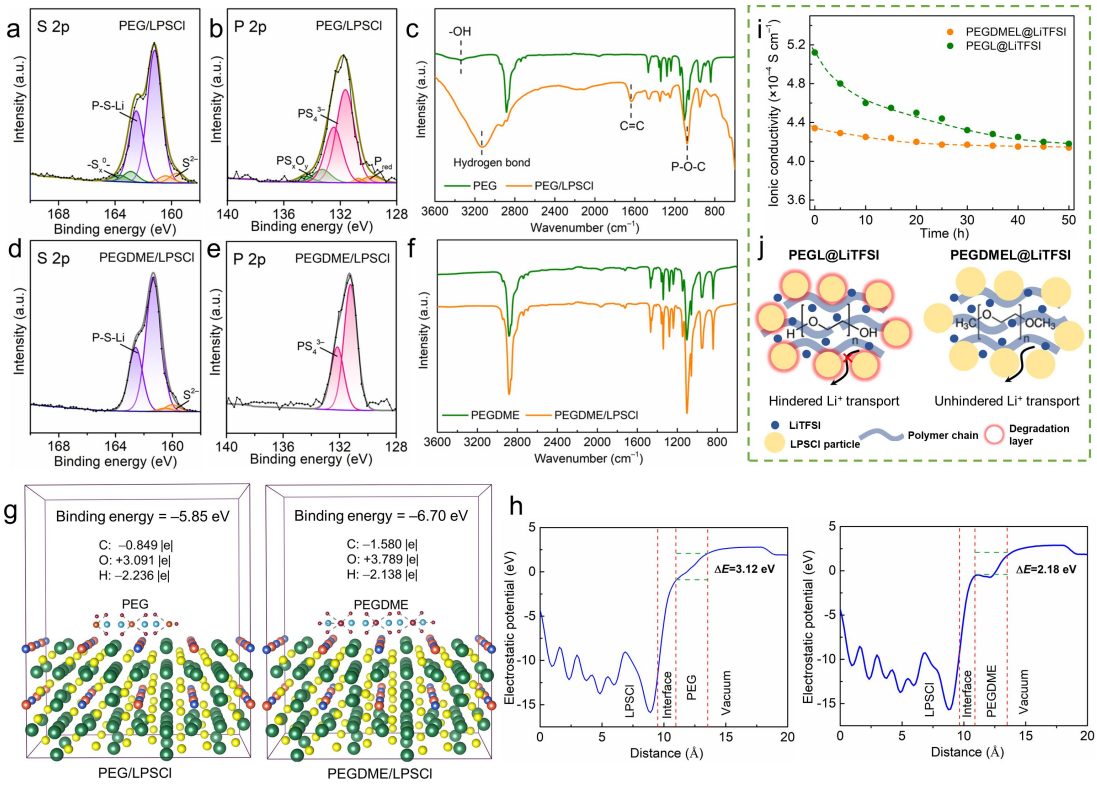

Figure 1. a) S 2p and b) P 2p XPS spectra of the PEG/LPSCl composite. c) FT-IR spectrum of the PEG/LPSCl composite. d) S 2p and e) P 2p XPS spectra of the PEGDME/LPSCl compound. f) FT-IR spectrum of the PEGDME/LPSCl compound. g) Atomic structures of PEG/LPSCl and PEGDME/LPSCl along with their respective binding energy and Bader charge results. h) Electrostatic potential profiles for the PEG/LPSCl and PEGDME/LPSCl. i) Time-dependent ionic conductivities of the PEGL@LiTFSI and PEGDMEL@LiTFSI at 60 °C. j) Schematic of the interface chemistry in the PEGL@LiTFSI and PEGDMEL@LiTFSI.

that the –OH group in the PEG disappears and hydrogen bonds and P–O–C bonds are observed after mixing with LPSCl (Figure 1c). In addition, the new peak at ≈1670 cm^{-1} indicates the formation of C=C groups, which corresponds to the reduction of the PEG polymer. The deprotonation process of PEO (PEG) is explained by various fragmentation reactions.[29,30] These reaction products are typical for thiophosphate-type SEs as not only LPSCl, but also Li_3PS_4 (with only PS_4^{3-} anions) shows such degradation products when mixing with PEG (Figure S4a and S4b), indicating general chemical instability of thiophosphate SEs in contact with PEG-type polymers.

Improved chemical stability between PEGDME and LPSCl

We speculate that the terminal –OH group in the PEG with high polarity triggers a series of side reactions between the LPSCl and PEG.[5] To prove this hypothesis, polyethylene glycol dimethyl ether (PEGDME) with substituted $–OCH_3$ terminal groups was mixed with LPSCl at 100 °C. In sharp contrast to the PEG/LPSCl mixture, the PEGDME/LPSCl mixture shows excellent chemical stability due to the decreased polarity of PEGDME. The peaks corresponding to LPSCl and PEGDME in the XPS and FT-IR spectra (Figure 1d–f) render no obvious change compared to the individual materials (Figure S4c and S4d).

DFT simulations were used to further confirm the improved chemical stability at the PEGDME/LPSCl interface compared to the PEG/LPSCl interface. The atom number for simulation of the PEG/LPSCl interface is 225, while the atom number of the PEGDME/LPSCl interface is 231. As shown in Figure 1g, the binding energy of the PEGDME/LPSCl interface (−6.70 eV) is lower than that of PEG/LiPSCl (−5.85 eV), indicating better stability of the PEGDME/LPSCl interface. The Bader charge, which is based purely on the electronic charge density, was performed to explore the cause of the differences regarding binding energy.[31] The results reveal that Li and P atoms from LPSCl, and C and H atoms from PEG/PEGDME lose electrons, while S and Cl atoms from LPSCl, and O atoms from PEG/PEGDME gain electrons. At the PEG/LPSCl interface, Li, P, C and H atoms lose 6.030|e|, 5.147|e|, 0.849|e|, and 2.236|e|, respectively, while S, Cl, and O atoms gain 13.816|e|, 7.039|e|, and 3.091|e|. In contrast, more charge transfer of PEGDME is obtained at the PEGDME/LPSCl interface due to the substituted terminal group (Li: −6.995|e|, P: −5.936|e|, C: −1.580|e|, H: −2.138|e|, S: 14.356|e|, Cl: 7.129|e|, and O: 3.789|e|). The electrostatic potential profiles in Figure 1h also exhibit a lower energy barrier at the PEGDME/LPSCl interface for

the electron transport. These results indicate that PEGDME adsorbs stronger on the LPSCl surface compared to PEG, thus achieving a more stable interface.[32] In addition, the interface stability at elevated temperatures was evaluated by the radial distribution function (RDF) (Figure S5). The RDF are similar at 273.15 K, 303.15 K and 373.15 K for both PEG/LPSCl and PEGDME/LPSCl interfaces, indicating ordered structures of polymers at short-range and long-range distances. Even if PEG may exhibit more severe side reactions with LPSCl at elevated temperature, the side reactions do not change the molecular segment stability of PEG. This could be attributed to the bonding association between PEG and LPSCl according to the FT-IR results.

Although interfacial degradation does not change the molecular segment stability of PEG, it greatly affects the ionic conductivities of composite SEs. A mixture of 85 wt % of LPSCl and 15 wt % of polymer was mixed with LiTFSI (EO:Li = 10) in a mortar at 60 °C for 30 min. Then the compound was calendered into thin SE sheets. The thin electrolytes with PEG and PEGDME polymer are abbreviated as PEGL@LiTFSI and PEGDMEL@LiTFSI, respectively. Originally, the ionic conductivity of PEGL@LiTFSI is $5.1\times10^{-4}\,S\,cm^{-1}$ at 60 °C (Figure 1i). It gradually decreases to $4.2\times10^{-4}\,S\,cm^{-1}$ after 50 h. This is ascribed to the continuous formation of an interface passivation layer, causing hindered Li^+ transport at the PEG/LPSCl interface (Figure 1j). Although the PEGDMEL@LiTFSI initially exhibits lower ionic conductivity ($4.3\times10^{-4}\,S\,cm^{-1}$ at 60 °C), the better PEGDME/LPSCl interfacial stability still keeps the original ionic conductivity after 60 h (Figure 1i and 1j).

Fabrication of PEGDMEL@mix thin composite SEs

Many thin thiophosphate SEs have been reported recently.[33] However, most of them cannot directly work with lithium anodes due to the thermodynamic instability of thiophosphates with lithium metal. Therefore, not only the polymer/thiophosphate interface inside the composite SEs, but also the Li/SE interface should be carefully designed when lithium metal is used as the anode. Inspired by rational SEI design in liquid-electrolyte batteries, LiFSI is introduced in the composite SEs to prevent side reactions and suppress lithium dendrite growth. During the initial resting time of the cell after fabrication and the following lithium plating/stripping process, a LiF-rich SEI can be formed due to the reaction of the LiFSI with lithium metal.[23] However, PEGDME/LiFSI shows poor ionic conduction because of the high crystallinity of the PEGDME (Figure S6a). In contrast, LiTFSI can decrease the crystallinity of PEGDME, thus enhancing the Li^+ transport ability (Figure S6b). Therefore, both LiTFSI and LiFSI salts (molar ratio = 1:1) were added to the PEGDME polymer, causing sufficient ionic conductivity as well as forming a LiF-rich interface in contact with lithium metal. The obtained composite SE is abbreviated as PEGDMEL@mix.

PEGDMEL@mix samples with various polymer concentrations (10, 15, 20, 25 wt %) were fabricated by solvent-free hot calendering. PEGDMEL@mix with 10 wt % PEGDME (PEGDMEL@mix(10 %)) shows a thickness of ≈100 μm, while PEGDMEL@mix with higher polymer content shows a thickness of ≈60 μm (Figure 2a–d). Mechanically pressed LPSCl pellets usually retain about 10–15 % porosity.[34] 10 wt % PEGDME is not enough to totally fill the pores between LPSCl particles, which makes the preparation of thinner layers more difficult. The enlarged cross-sectional SEM image confirms a porous structure of the PEGDMEL@mix(10 %) (Figure S7a). In contrast, PEGDMEL@mix(15 %, 20 % and 25 %) have a dense structure, indicating that all pores are filled (Figure S7b–d). EDS mappings in Figure S8 confirm the composite structure. Plane-view SEM images show that the PEGDMEL@mix-(15 %) exhibits the smoothest surface compared to PEGDMEL@mix(20 %) and PEGDMEL@mix(25 %) (Figure S9).

The homogeneity of the PEGDMEL@mix(15 %) was examined by TOF-SIMS. TOF-SIMS depth profiling reveals the composition of fragments from the sample during the sputtering process.[35] Here, PS^-, SNO^-, CHO_3^- fragments stem from the LPSCl, LiTFSI/LiFSI salt, and PEGDME, respectively. As shown in Figure 2e, SNO^- and CHO_3^- signals show high intensities at the beginning. Their intensities gradually decrease until keeping constant after 15 s. The PS^- signal shows the opposite trend, i.e. its intensity gradually increases from a low level until remaining stable after 15 s. This reveals the PEGDME enrichment at the surface and a homogeneous composite structure in the bulk. In addition, TOF-SIMS chemical mapping (Figure 2f) and 3D views of the sputtered volume (Figure S10) show a strong CHO_3^- signal but little PS^- signal at the surface, further confirming the PEGDME-rich surface. In the bulk of PEGDMEL@mix(15 %), PEGDME is distributed between LPSCl particles, while LiTFSI/LiFSI salt is homogeneously distributed in the PEGDME phase (Figure 2g). The LiFSI at the PEGDME-rich surface can form a LiF-rich SEI to suppress lithium dendrite growth when contacting with lithium. Moreover, the LiFSI in the bulk PEGDME can consume the lithium dendrites even if they penetrate the electrolyte through the LiF-rich SEI, thus achieving double protection.

The conductivities of PEGDMEL@mix SEs with various polymer fractions were characterized by EIS. PEGDMEL@mix(15 %) exhibits the highest ionic conductivity of $4.5\times10^{-5}\,S\,cm^{-1}$ at 25 °C and of $2.4\times10^{-4}\,S\,cm^{-1}$ at 60 °C (Figure 2h and Figure S11). Temperature-dependent EIS was measured from 20 °C to 80 °C and the activation energy (E_a) was calculated from the Arrhenius plot (Figure 2i and Figure S12). For PEGDMEL@mix(15 %) we obtain $E_a = 0.44$ eV, which is slightly higher than that of the LPSCl pellet. Figure 2j shows that the Li^+ transference number (t_+) of PEGDMEL@mix(15 %) is 0.54. This relatively high t_+ is beneficial for uniform Li^+ deposition due to the increased fraction of fixed anions.[36] As PEGDMEL@mix(15 %) has the best ionic conductivity among the tested polymer/salt ratios, hereafter, PEGDMEL@mix refers to PEGDMEL@mix(15 %) unless otherwise stated.

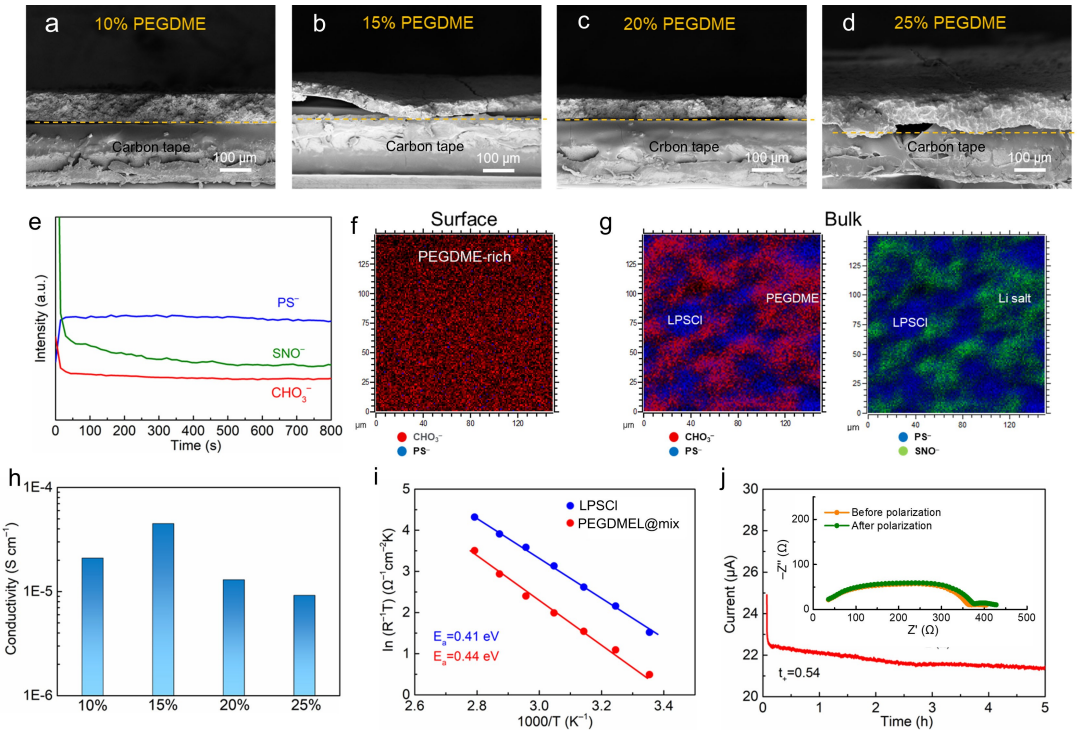

Figure 2. Cross-sectional SEM images of the PEGDMEL@mix electrolytes with the PDGDME content of a) 10%, b) 15%, c) 20% and d) 25%, respectively. e) TOF-SIMS depth profiles for the PEGDMEL@mix. TOF-SIMS chemical mappings (f) at the surface and (g) in the bulk of the PEGDMEL@mix(15%). h) Ionic conductivities of PEGDMEL@mix electrolytes with various PDGDME contents. i) Arrhenius plot of LPSCl and PEGDMEL@mix(15%). j) Experimental determination t_+ of the PEGDMEL@mix(15%).

Characterizations of in situ formed LiF-rich SEI

In situ XPS was employed to investigate the SEI components when PEGDMEL@mix is brought into contact with lithium.[37] The experimental setup is sketched in Figure 3a. An argon ion gun was used to sputter the lithium on the PEGDMEL@mix for 5 min followed by recording of the XPS spectra. Sequential lithium deposition and XPS measurements were performed, leading to a set of spectra as a function of the deposition time. Figure 3b–d show the waterfall plots of the F 1s, S 2p, and O 1s signals, respectively. The corresponding fitting mode can be found in Figure S13. During initial lithium deposition ($t<10$ min), the decomposition of LiFSI is indicated by the disappearance of the $-SO_2F$ (F 1s, S 2p) signals with time. Simultaneously, the LiF (F 1s) and $Li_xS_yO_z$ (S 2p, O 1s) signal intensities are increased. They are decomposition products of LiFSI according to the following reaction [Eq. (1)].[38]

$$LiN(SO_2F)_2 + 6Li \rightarrow Li_3N + Li_2S_2O_4 + 2LiF \quad (1)$$

Note that LiTFSI may also contribute to LiF formation due to the decreasing $-CF_3$ (F 1s) and $-SO_2CF_3$ (S 2p) signals.[39] The polysulfide signal ($-S_x^0-$) originates from the oxidative dimerization of the PS_4^{3-} tetrahedral units [Eq. (2) or (3)].[24]

$$2PS_4^{3-} \rightarrow P_2S_7^{4-} + S + 2e^- \quad (2)$$

$$2PS_4^{3-} \rightarrow P_2S_6^{2-} + 2S + 4e^- \quad (3)$$

And a subsequent reduction of $Li_2S_2O_4$ and polysulfides lead to the formation of Li_2S and Li_2O [Eq. (4) and (5)].

$$Li_2S_2O_4 + 10Li \rightarrow 2Li_2S + 4Li_2O \quad (4)$$

$$S_x^0 + 2xLi \rightarrow xLi_2S \quad (5)$$

After initial lithium deposition ($t>15$ min), LiF, Li_2S and Li_2O show dominant intensity, and they primarily compose the SEI on the surface of the PEGDMEL@mix.

To evaluate the Li/SE interface stability, Li/LPSCl/Li and Li/PEGDMEL@mix/Li cells were assembled and time-dependent EIS was applied (one measurement every hour. Figure 3e shows the Nyquist plots of the Li/LPSCl/Li cell immediately after assembly. The resistance at high frequency corresponds to the SE resistance (R_{SE}) of LPSCl. $R_{SE}=62.8\,\Omega cm^2$ is consistent with the ionic conductivity of the LPSCl pellet at 25 °C. The resistance at middle frequency corresponds to the Li/LPSCl interface resistance ($R_{interface}$) and interphase resistance ($R_{interphase}$) due to the degradation between Li and LPSCl (Figure S14a). The temporal evolution of the interface related resistance ($R_{re\text{-}inter}$) is shown in Figure 3g, which corresponds to the sum of $R_{interface}$ and $R_{interphase}$, whereas the corresponding individual changes of $R_{interface}$ and $R_{interphase}$ can be found in Figure S15. The initial $R_{re\text{-}inter}$ is 152.2 Ωcm^2 and increases to 633.8 Ωcm^2

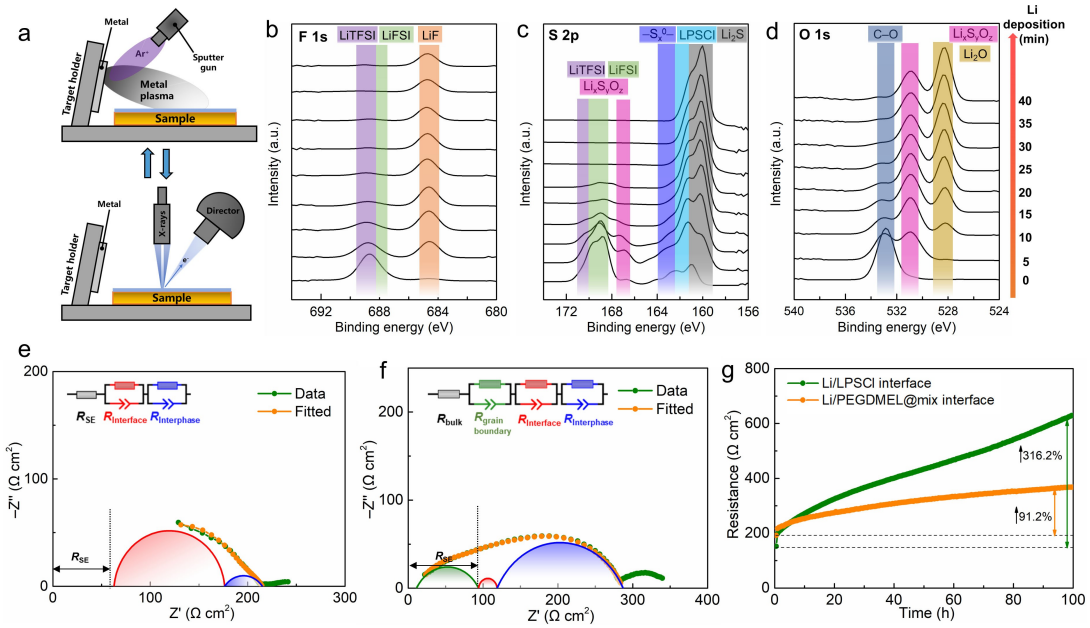

Figure 3. a) Schematic illustration of in situ XPS with lithium deposition. In situ XPS spectra of b) F 1s, c) S 2s, and d) O 1s at different lithium deposition time. EIS spectra with representative fits of e) Li/LPSCl/Li and f) Li/PEGDMEL@mix/Li cells after assembly. g) Temporal evolution of the fitted resistances at the Li/LPSCl and Li/PEGDMEL@mix interfaces.

after 100 h, rendering a 316.2 % change. The greatly increased $R_{\text{re-inter}}$ results from the continuous side reactions between the LPSCl and lithium, which hinder Li^+ migration at the interface. Nyquist plots of the Li/PEGDMEL@mix/Li cell were fitted using a modified equivalent circuit, where bulk resistance (R_{bulk}) and grain boundary resistance ($R_{\text{grain boundary}}$) together contribute to the R_{SE} (Figure 3f). The $R_{\text{SE}} = 94.2\ \Omega\,\text{cm}^2$ agrees with the ionic conductivity of PEGDMEL@mix. The $R_{\text{re-inter}}$ of Li/PEGDMEL@mix shows a 91.2 % increase and keeps relatively constant after 100 h (Figure 3g). This increase is attributed to the formed LiF-rich SEI as its low ionic conductivity blocks the Li^+ transport. However, the increase is much smaller than that of the $R_{\text{re-inter}}$ of LPSCl (316.2 %). The increase of the $R_{\text{re-inter}}$ of Li/PEGDMEL@mix slows down with time, indicating the prevention of interfacial degradation by the LiF-rich SEI (Figure S14b).

Electrochemical performance of PEGDMEL@mix SEs

The CE of lithium plating/stripping is a sensitive indicator for Li/SE interface stability and lithium dendrite growth. The CEs based on the LPSCl and PEGDMEL@mix SEs were evaluated by Li/SE/ stainless steel (SS) half cells, where SS served as current collector. The lithium plating/striping of the Li/LPSCl/SS cell shows an overpotential of 28.3 mV with an initial CE of 91.2 % (Figure 4a). The CE increases to 94.4 % after 5 activation cycles. Then the CE gradually decreases to 86.2 % after 17 cycles, which is attributed to continuous lithium consumption by interfacial side reactions and lithium dendrite growth. The following cycles show unstable CEs with a large fluctuation, indicating the short-circuit of the Li/LPSCl/SS cell. FIB-SEM was employed to investigate the interface after cycling. A cryo-stage was used to decrease any damage to the samples as much as possible during the FIB cutting process, considering that lithium metal and polymer are sensitive to both ion and electron beams. A porous dead lithium layer is observed between the SS layer and the LPSCl pellet (Figure 4d). The observation of a partly irreversible lithium deposition not only explains the low CEs, but also facilitates lithium dendrite growth. The lithium dendrite penetration in the LPSCl pellet is also clearly observed, thus shorting the Li/LPSCl/SS cell.

In contrast, the Li/PEGDMEL@mix/SS cell exhibits a lower initial CE (87.6 %) and a larger overpotential (0.14 V) than the Li/LPSCl/SS cell (Figure 4b). However, the CE increases to ≈98 % after several activation cycles and remains stable after 50 cycles (Figure 4c). As apparently only a little irreversible lithium is formed, the SS current collector is easily separated from the cell after cycling. Therefore, a thin platinum layer was sputtered to protect the surface of the PEGDMEL@mix before FIB cutting. The cross-sectional FIB-SEM back scattered electron (BSE) image in Figure 4e shows a thin LiF-rich SEI and dendrite-free PEGDMEL@mix SE. Energy dispersive X-ray spectroscopy (EDS) shows an increased LiF signal at the Li/PEGDMEL@mix interface compared to the Li/LPSCl interface (Figure S16 and S17). Note that the PEGDMEL@mix is thinner by one order of magnitude than the LPSCl pellet (Figure 4f). The much improved cycle stability with high CE of Li/PEGDMEL@mix/SS cells benefits from the prevention of interfacial degradation and the suppression of lithium dendrite growth at the interface.

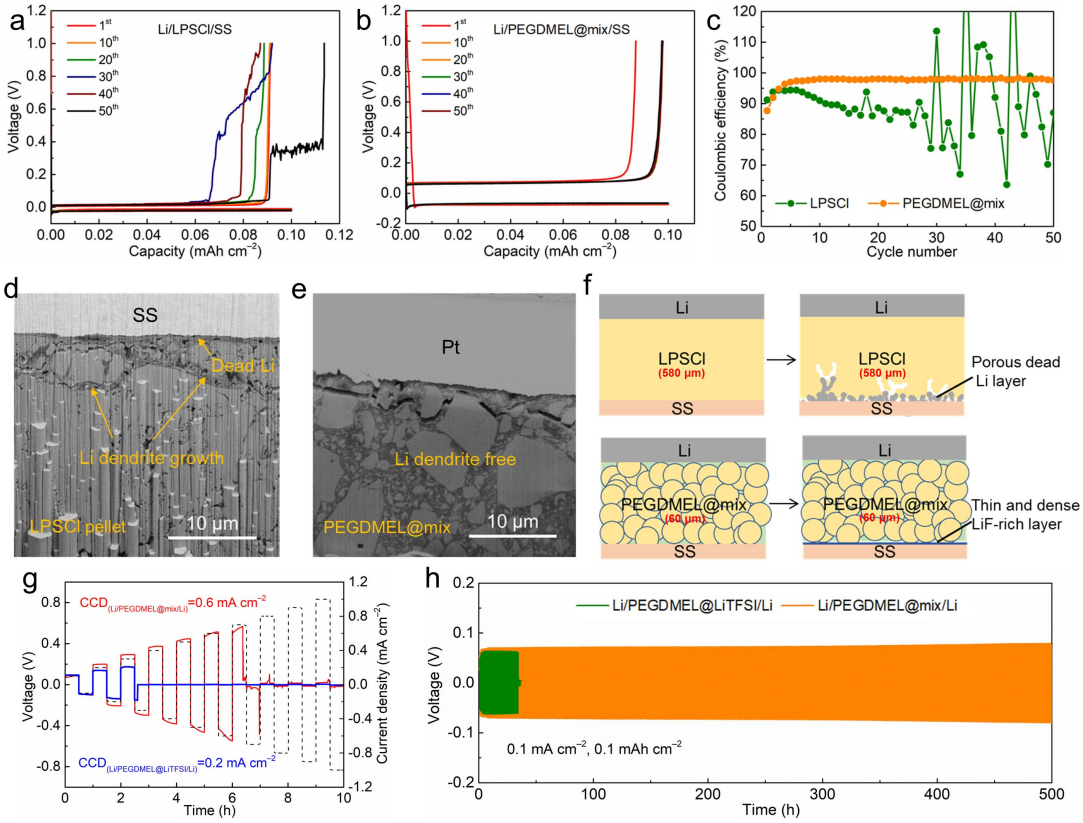

Figure 4. Li plating/stripping profiles on an SS working electrode using a) LPSCl as the SE, and b) PEGDMEL@mix as the SE at 0.1 mA cm^{-2}. c) CEs of the Li/LPSCl/Cu and Li/PEGDMEL@mix/Cu cells. FIB-SEM BSE images of the d) Li/LPSCl/Cu and e) Li/PEGDMEL@mix/Cu cells after 50 cycles at 0.1 mA cm^{-2}. f) Schematic illustration of different Li plating/stripping based on LPSCl and PEGDMEL@mix electrolytes. g) CCD of the Li/PEGDMEL@mix/Li and the Li/PEGDME@LiTFSI/Li cells. h) Galvanostatic cycling performance of the Li/PEGDMEL@mix/Li and the Li/PEGDME@LiTFSI/Li cells at 0.1 mAcm^{-2} (0.1 mAh cm^{-2}) at 25 °C.

The critical current density (CCD) is also regarded as a measure of the interfacial stability and the dendrite suppression capability. The obtained CCD values vary with applied current densities and capacities, which is defined as the maximum current density before a short-circuit.[40] Here, the current density was increased for each step starting with 0.1 mA cm^{-2}, and the time of plating/stripping was set to 0.5 h per step. Both the PEGDMEL@mix and PEGDME@LiTFSI electrolytes show the same thickness of 60 μm. However, the CCD of the Li/PEGDMEL@mix/Li cell is 0.6 mA cm^{-2}, which is higher than that of the Li/PEGDMEL@LiTFSI/Li cell (0.2 mA cm^{-2}) (Figure 4f). Galvanostatic lithium plating/stripping experiments were carried out to evaluate the long-term cycling stability. The Li/PEGDME@LiTFSI/Li cell shorts after 33 h of cycling at 0.1 mA cm^{-2} (0.1 mAh cm^{-2}). In sharp contrast, a continuous cycling for 600 h is obtained for the Li/PEGDMEL@mix/Li cell (Figure 4f and Figure S18). Moreover, the Li/PEGDMEL@mix/Li cell cycles for 350 h at an increased current density of 0.2 mA cm^{-2} (Figure S19).

The electrochemical stability window (ESW) is a key parameter for SEs. High oxidation of SEs enables the use of high-voltage CAMs, and thus raises the energy density of SSBs. Cells of the Li–In/SE/C-coated Al foil were assembled, and linear sweep voltammetry (LSV) was employed to estimate the ESW. The inflection point is defined as the onset oxidation voltage during LSV scan. The Li–In anode can minimize the interference of side reactions at the anode side compared to a lithium metal anode. For better comparison, the following potentials are stated relative to the Li^+/Li potential by taking into account that 0 V vs. In/InLi corresponds to 0.62 V vs. Li^+/Li. As shown in Figure 5a, the ESW of PEGDMEL@mix is 4.6 V, which is due to the high ESW of PEGDME. In contrast, PEG shows a narrow ESW of 4.0 V, which is consistent with previous studies. PEO-based SEs cannot work with $LiCoO_2$ due to severe interfacial degradation and gas release when charging to 4.2 V.[41] Considering that PEG and PEGDME shows the same polymer backbone (i.e. $-(O-CH_2-CH_2)_n-$), the difference of the ESW between them comes from the different terminal groups. The -OCH_3 group in PEGDME not only leads to better stability with LPSCl, but also causes a better high-voltage capability than the -OH group in the PEO.[42]

Full SSB cells with a $LiNi_{0.85}Co_{0.1}Mn_{0.05}O_2$ (NCM) cathode and lithium anode were constructed using PEGDMEL@mix SE. The surface of the NCM particles was coated with a thin layer of $LiNbO_3$ (LNbO) to prevent the electrochemical degradation at the NCM/LPSCl interface.[43] The FIB-SEM BSE image in Figure S20 confirms homogeneously distributed NCM@LNbO particles in the LPSCl

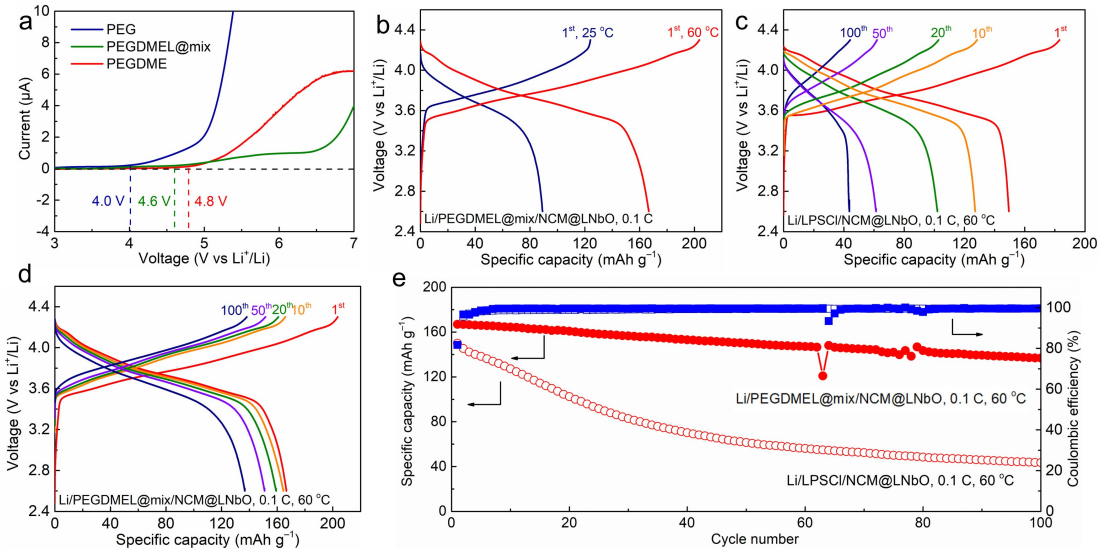

Figure 5. a) LSV of various SEs. b) The first charge/discharge curves of the Li/PEGDMEL@mix/NCM@LNbO cell at 25 °C and 60 °C. c) The charge/discharge curves of the Li/LPSCl/NCM@LNbO cell at 0.1 C (d) The charge/discharge curves of the Li/PEGDMEL@mix/NCM@LNbO cell at 0.1 C. e) Cycle performance of the Li/LPSCl/NCM@LNbO and Li/PEGDMEL@mix/NCM@LNbO at 0.1 C. The applied temperature is 60 °C and the pressure is 14 MPa.

matrix, thus ensuring fast Li^+ transport. The initial specific capacity of the Li/PEGDMEL@mix/NCM@LNbO cell increases from 89.1 mAh g^{-1} to 166.5 mAh g^{-1} at 0.1 C when increasing the temperature from 25 °C to 60 °C, which is attributed to the enhanced ionic conductivity of PEGDMEL@mix at 60 °C (Figure 5b). However, the Li/LPSCl/NCM@LNbO cell delivers a slightly lower initial specific capacity of 149.4 mAh g^{-1} at 0.1 C even if the LPSCl exhibits higher ionic conductivity at 60 °C (Figure 5c). The result comes from the side reactions at the Li/LPSCl interface. The continuously deteriorating Li/LPSCl interface leads to a low specific capacity of 43.6 mAh g^{-1} after 100 cycles (Figure 5e). The Li/PEGDMEL@mix/NCM@LNbO cell with LiF-rich SEI shows a higher capacity retention of 81.2 % after 100 cycles (Figure 5d and e). In contrast, the Li/PEGDME@LiTFSI/NCM@LNbO cell shorts after only 5 cycles (Figure S21). In addition, the molten PEGDME can infiltrate into the composite cathode to improve the contact loss during repeated cycling, thus ensuring excellent cycling stability.

General design of analogous composite SEs with Cl-rich LPSCl and LGPS

An ideal thin SE separator should simultaneously achieve a low thickness (< 60 μm), high ionic conductivity (> 10^{-4} S cm^{-1} at 25 °C), large electrochemical window (> 4.5 V), and excellent electrode/SE interfacial stability.[21,44] The designed PEGDMEL@mix shows an ionic conductivity of 4.5×10^{-5} S cm^{-1} at 25 °C, which is insufficient for practical applications. Finding alternative SE fillers with higher ionic conductivity is a promising method to improve the ionic conductivity of composite SEs. Nazar and co-workers reported new halide-rich solid solution phases in the argyrodite-type LPSCl family $Li_{6-x}PS_{5-x}Cl_{1+x}$.[45] The substitution of divalent S^{2-} by monovalent Cl^- leads to weakened interactions between the mobile Li^+ and surrounding framework anions, thus enhancing the ionic conductivity. $Li_{5.5}PS_{4.5}Cl_{1.5}$ (Cl-rich LPSCl) pellets show an ionic conductivity of 5.2×10^{-3} S cm^{-1} at 25 °C, which is five-fold greater than stoichiometric LPSCl (Figure S22a). The PEGDMEL@mix with Cl-rich LPSCl exhibits an improved ionic conductivity of 8.0×10^{-5} S cm^{-1} at 25 °C (Figure S22c). In addition, LGPS with a one-dimensional (1D) lithium conduction pathway was also used to fabricate thin composite SEs.[46] The ionic conductivity of fabricated composite SEs can reach 1.6×10^{-4} S cm^{-1} at 25 °C, which benefits from the high ionic conductivity of LGPS (Figure S22b and S22c). However, LGPS shows severe side reactions with lithium due to the reduction of germanium.[26] An electron-conducting interphase leads to a gradually increased overpotential of the Li/LGPS/Li cell cycling at 0.2 mA cm^{-2}. In contrast, the composite SE with LiF-rich SEI can suppress the interfacial degradation, enabling stable cycling for 450 h at 0.2 mA cm^{-2} (Figure S23).

High pressure (e.g. 70 MPa) is usually applied for SSBs with Li–In anodes to maintain good interfacial contact between NCM particles and the LPSCl matrix in the composite cathode.[9] However, this process can induce physical short-circuits of SSBs with lithium anodes due to lithium creep, even if 500 μm thick LPSCl pellets are used as SEs.[47] A relatively low pressure of 14 MPa in this paper inevitably causes a faster capacity decay of the Li/LPSCl/NCM@LNbO cell due to the contact loss in the composite NCM cathode during repeated cycling, along with the degraded anode interface. However, the Li/PEGDMEL@mix/NCM@LNbO cell exhibits excellent cycling stability at

60 °C. The molten PEGDEM from the PEGDMEL@mix can infiltrate into the pores of the composite cathode to ensure fast Li^+ transport, while LPSCl as the major component retains an intact SE skeleton. The wetted cathode design is widely applied in industry to fabricate solid–liquid hybrid batteries, especially with thick cathodes. More research will focus on the interfaces at the cathode part, where the optimization of the cathode structure is required for all-solid-state batteries.

Conclusion

In summary, interfaces of thin polymer/thiophosphate SEs are rationally designed to improve dendrite-free lithium metal batteries. PEG with high polarity triggers polymerization reactions of PS_4^{3-} units in the LPSCl, thus decreasing the ionic conductivity of composite SEs. PEGDEM with a substituted terminal group modified from -OH to -OCH_3 can stabilize the PEGDEM/LPSCl interface, while a LiF-rich SEI formed by introduction of mixed lithium salt can stabilize the Li/SE interface. The solvent-free PEGDMEL@mix composite electrolyte was prepared as a thin layer with a thickness of 60 μm and ionic conductivity of 4.5×10^{-5} S cm^{-1} at 25 °C. The ionic conductivity was improved to over 10^{-4} S cm^{-1} by introducing LGPS fillers. A LiF-rich SEI was proven by in situ XPS, which exhibits homogeneous lithium plating/stripping, leading to a CE over 98 % for Li/PEGDMEL@mix/SS cells and 500 h stable cycling for Li/PEGDMEL@mix/Li cells at 0.1 mA cm^{-1}. The Li/PEGDMEL@mix/NCM@LNbO cell shows a capacity retention of 81.2 % after 100 cycles at 60 °C. The improved cycling stability results from the LiF protected lithium interface and a stable cathode interface by molten PEGDEM infiltration. This work highlights the chemical compatibility of thiophosphate SEs in the design of polymer/thiophosphate composite SEs. The thin composite SEs with interfacial stability potentially facilitate dendrite-free lithium metal batteries with high energy density.

Acknowledgements

The authors acknowledge financial support from the Federal Ministry of Education and Research (BMBF, Bundesministerium für Bildung und Forschung) within the FESTBATT consortium (03XP0430A), and NSERC, University of Toronto and Compute Canada. Open Access funding enabled and organized by Projekt DEAL.

Conflict of Interest

The authors declare no conflict of interest.

Data Availability Statement

The data that support the findings of this study are available from the corresponding author upon reasonable request.

Keywords: Interfacial Stability · Lithium Dendrite Suppression · Protection Layer · Solid Electrolyte Separators · Terminal Group

[1] J.-M. Tarascon, M. Armand, *Nature* **2001**, *414*, 359; M. Armand, J.-M. Tarascon, *Nature* **2008**, *451*, 652–657.
[2] a) T. Krauskopf, F. H. Richter, W. G. Zeier, J. Janek, *Chem. Rev.* **2020**, *120*, 7745; b) C. Wang, K. Fu, S. P. Kammampata, D. W. McOwen, A. J. Samson, L. Zhang, G. T. Hitz, A. M. Nolan, E. D. Wachsman, Y. Mo, V. Thangadurai, L. Hu, *Chem. Rev.* **2020**, *120*, 4257; c) X. B. Cheng, R. Zhang, C. Z. Zhao, Q. Zhang, *Chem. Rev.* **2017**, *117*, 10403.
[3] a) S. Randau, D. A. Weber, O. Kötz, R. Koerver, P. Braun, A. Weber, E. Ivers-Tiffée, T. Adermann, J. Kulisch, W. G. Zeier, F. H. Richter, J. Janek, *Nat. Energy* **2020**, *5*, 259; b) Y. Chen, Z. Wang, X. Li, X. Yao, C. Wang, Y. Li, W. Xue, D. Yu, S. Y. Kim, F. Yang, *Nature* **2020**, *578*, 251; c) Q. Zhao, S. Stalin, C.-Z. Zhao, L. A. Archer, *Nat. Rev. Mater.* **2020**, *5*, 229.
[4] P. P. Paul, B.-R. Chen, S. A. Langevin, E. J. Dufek, J. N. Weker, J. S. Ko, *Energy Storage Mater.* **2022**, *45*, 969–1001.
[5] J. Wu, S. Liu, F. Han, X. Yao, C. Wang, *Adv. Mater.* **2021**, *33*, 2000751.
[6] a) K. H. Park, Q. Bai, D. H. Kim, D. Y. Oh, Y. Zhu, Y. Mo, Y. S. Jung, *Adv. Energy Mater.* **2018**, *8*, 1800035; b) L. Zhou, N. Minafra, W. G. Zeier, L. F. Nazar, *Acc. Chem. Res.* **2021**, *54*, 2717–2728.
[7] J. Kasemchainan, S. Zekoll, D. Spencer Jolly, Z. Ning, G. O. Hartley, J. Marrow, P. G. Bruce, *Nat. Mater.* **2019**, *18*, 1105.
[8] Z. Ning, D. S. Jolly, G. Li, R. De Meyere, S. D. Pu, Y. Chen, J. Kasemchainan, J. Ihli, C. Gong, B. Liu, *Nat. Mater.* **2021**, *20*, 1121–1129.
[9] R. Koerver, I. Aygün, T. Leichtweiß, C. Dietrich, W. Zhang, J. O. Binder, P. Hartmann, W. G. Zeier, J. Janek, *Chem. Mater.* **2017**, *29*, 5574.
[10] W. Zhang, T. Leichtweiß, S. P. Culver, R. Koerver, D. Das, D. A. Weber, W. G. Zeier, J. Janek, *ACS Appl. Mater. Interfaces* **2017**, *9*, 35888.
[11] F. Walther, S. Randau, Y. Schneider, J. Sann, M. Rohnke, F. H. Richter, W. G. Zeier, J. Janek, *Chem. Mater.* **2020**, *32*, 6123.
[12] X. Li, Z. Ren, M. Norouzi Banis, S. Deng, Y. Zhao, Q. Sun, C. Wang, X. Yang, W. Li, J. Liang, *ACS Energy Lett.* **2019**, *4*, 2480.
[13] F. Walther, R. Koerver, T. Fuchs, S. Ohno, J. Sann, M. Rohnke, W. G. Zeier, J. Janek, *Chem. Mater.* **2019**, *31*, 3745.
[14] a) H. Wan, S. Liu, T. Deng, J. Xu, J. Zhang, X. He, X. Ji, X. Yao, C. Wang, *ACS Energy Lett.* **2021**, *6*, 862; b) F. Zhao, Q. Sun, C. Yu, S. Zhang, K. Adair, S. Wang, Y. Liu, Y. Zhao, J. Liang, C. Wang, *ACS Energy Lett.* **2020**, *5*, 1035; c) F. Han, J. Yue, X. Zhu, C. Wang, *Adv. Energy Mater.* **2018**, *8*, 1703644.
[15] a) R. S. Negi, Y. Yusim, R. Pan, S. Ahmed, K. Volz, R. Takata, F. Schmidt, A. Henss, M. T. Elm, *Adv. Mater. Interfaces* **2021**, *8*, 2101428; b) Y.-J. Kim, R. Rajagopal, S. Kang, K.-S. Ryu, *Chem. Eng. J.* **2020**, *386*, 123975; c) D. Kitsche, Y. Tang, Y. Ma, D. Goonetilleke, J. Sann, F. Walther, M. Bianchini, J. Janek, T. Brezesinski, *ACS Appl. Energy Mater.* **2021**, *4*, 7338.
[16] H.-K. Tian, Z. Liu, Y. Ji, L.-Q. Chen, Y. Qi, *Chem. Mater.* **2019**, *31*, 7351.
[17] a) S. Sen, E. Trevisanello, E. Niemöller, B.-X. Shi, F. J. Simon, F. H. Richter, *J. Mater. Chem. A* **2021**, *9*, 18701; b) X. Yang, X. Gao, M. Jiang, J. Luo, J. Yan, J. Fu, H. Duan, S. Zhao, Y.

Tang, R. Yang, R. Li, J. Wang, H. Huang, X. Sun, C. V. Singh, *Angew. Chem. Int. Ed.* **2023**, *62*, e202215680; *Angew. Chem.* **2023**, *135*, e202215680.
[18] S. Luo, Z. Wang, A. Fan, X. Liu, H. Wang, W. Ma, L. Zhu, X. Zhang, *J. Power Sources* **2021**, *485*, 229325.
[19] X. Xu, G. Hou, X. Nie, Q. Ai, Y. Liu, J. Feng, L. Zhang, P. Si, S. Guo, L. Ci, *J. Power Sources* **2018**, *400*, 212.
[20] J. Zheng, P. Wang, H. Liu, Y.-Y. Hu, *ACS Appl. Energy Mater.* **2019**, *2*, 1452.
[21] M. Jia, N. Zhao, H. Huo, X. Guo, *Electrochem. Energy Rev.* **2020**, *3*, 656–689.
[22] C. Monroe, J. Newman, *J. Electrochem. Soc.* **2005**, *152*, A396; C. Brissot, M. Rosso, J.-N. Chazalviel, S. Lascaud, *J. Power Sources* **1999**, *81*, 925.
[23] X. Fan, X. Ji, F. Han, J. Yue, J. Chen, L. Chen, T. Deng, J. Jiang, C. Wang, *Sci. Adv.* **2018**, *4*, eaau9245.
[24] F. J. Simon, M. Hanauer, A. Henss, F. H. Richter, J. Janek, *ACS Appl. Mater. Interfaces* **2019**, *11*, 42186.
[25] a) J. Auvergniot, A. Cassel, D. Foix, V. Viallet, V. Seznec, R. Dedryvère, *Solid State Ionics* **2017**, *300*, 78; b) J. Auvergniot, A. Cassel, J.-B. Ledeuil, V. Viallet, V. Seznec, R. Dedryvère, *Chem. Mater.* **2017**, *29*, 3883.
[26] S. Wenzel, S. Randau, T. Leichtweiß, D. A. Weber, J. Sann, W. G. Zeier, J. Janek, *Chem. Mater.* **2016**, *28*, 2400.
[27] A. Maiti, P. Bhattacharyya, *Tetrahedron* **1994**, *50*, 10483; B. Bozzini, L. D'Urzo, C. Mele, V. Romanello, *J. Mater. Sci. Mater. Electron.* **2006**, *17*, 915.
[28] M. Li, M. Kolek, J. E. Frerichs, W. Sun, X. Hou, M. R. Hansen, M. Winter, P. Bieker, *ACS Sustainable Chem. Eng.* **2021**, *9*, 11314.
[29] N. Riphaus, B. Stiaszny, H. Beyer, S. Indris, H. A. Gasteiger, S. J. Sedlmaier, *J. Electrochem. Soc.* **2019**, *166*, A975.
[30] T. H. Hester, D. E. Castillo, D. J. Goebbert, *Rapid Commun. Mass Spectrom.* **2013**, *27*, 1643.
[31] Y. Xiang, M. Jiang, H. Xiao, K. Xing, X. Peng, S. Zhang, D.-C. Qi, *Appl. Surf. Sci.* **2019**, *496*, 143604.
[32] Q. Zhang, Y. Wang, Z. W. Seh, Z. Fu, R. Zhang, Y. Cui, *Nano Lett.* **2015**, *15*, 3780.
[33] a) C. Wang, R. Yu, H. Duan, Q. Lu, Q. Li, K. R. Adair, D. Bao, Y. Liu, R. Yang, J. Wang, *ACS Energy Lett.* **2022**, *7*, 410; b) Z. Zhang, L. Wu, D. Zhou, W. Weng, X. Yao, *Nano Lett.* **2021**, *21*, 5233; c) B. Emley, Y. Liang, R. Chen, C. Wu, M. Pan, Z. Fan, Y. Yao, *Mater. Today Phys.* **2021**, *18*, 100397; d) T. Jiang, P. He, Y. Liang, L.-Z. Fan, *Chem. Eng. J.* **2021**, *421*, 129965.
[34] J. M. Whiteley, P. Taynton, W. Zhang, S. H. Lee, *Adv. Mater.* **2015**, *27*, 6922.
[35] N. W. Li, Y. Shi, Y. X. Yin, X. X. Zeng, J. Y. Li, C. J. Li, L. J. Wan, R. Wen, Y. G. Guo, *Angew. Chem. Int. Ed.* **2018**, *57*, 1505; *Angew. Chem.* **2018**, *130*, 1521.
[36] H. Huo, Y. Chen, J. Luo, X. Yang, X. Guo, X. Sun, *Adv. Energy Mater.* **2019**, *9*, 1804004.
[37] S. Wenzel, T. Leichtweiss, D. Krüger, J. Sann, J. Janek, *Solid State Ionics* **2015**, *278*, 98.
[38] G. G. Eshetu, X. Judez, C. Li, M. Martinez-Ibañez, I. Gracia, O. Bondarchuk, J. Carrasco, L. M. Rodriguez-Martinez, H. Zhang, M. Armand, *J. Am. Chem. Soc.* **2018**, *140*, 9921.
[39] F. J. Simon, M. Hanauer, F. H. Richter, J. Janek, *ACS Appl. Mater. Interfaces* **2020**, *12*, 11713.
[40] a) Y. Lu, C. Z. Zhao, H. Yuan, X. B. Cheng, J. Q. Huang, Q. Zhang, *Adv. Funct. Mater.* **2021**, *31*, 2009925; b) B. Kinzer, A. L. Davis, T. Krauskopf, H. Hartmann, W. S. LePage, E. Kazyak, J. Janek, N. P. Dasgupta, J. Sakamoto, *Matter* **2021**, *4*, 1947.
[41] a) H. Huo, K. Huang, W. Luo, J. Meng, L. Zhou, Z. Deng, J. Wen, Y. Dai, Z. Huang, Y. Shen, *ACS Energy Lett.* **2022**, *7*, 650; b) Y. Yusim, E. Trevisanello, R. Ruess, F. H. Richter, A. Mayer, D. Bresser, S. Passerini, J. Janek, A. Henss, *Angew. Chem. Int. Ed.* **2023**, *62*, e202218316; *Angew. Chem.* **2023**, *135*, e202218316.
[42] X. Yang, M. Jiang, X. Gao, D. Bao, Q. Sun, N. Holmes, H. Duan, S. Mukherjee, K. Adair, C. Zhao, J. Liang, W. Li, J. Li, Y. Liu, H. Huang, L. Zhang, S. Lu, Q. Lu, R. Li, C. V. Singh, X. Sun, *Energy Environ. Sci.* **2020**, *13*, 1318.
[43] a) H. Yu, S. Wang, Y. Hu, G. He, I. P. Parkin, H. Jiang, *Green Energy Environ.* **2022**, *7*, 266–274; b) L. De Biasi, B. Schwarz, T. Brezesinski, P. Hartmann, J. Janek, H. Ehrenberg, *Adv. Mater.* **2019**, *31*, 1900985.
[44] N. Zhao, W. Khokhar, Z. Bi, C. Shi, X. Guo, L.-Z. Fan, C.-W. Nan, *Joule* **2019**, *3*, 1190.
[45] P. Adeli, J. D. Bazak, K. H. Park, I. Kochetkov, A. Huq, G. R. Goward, L. F. Nazar, *Angew. Chem.* **2019**, *131*, 8773.
[46] N. Kamaya, K. Homma, Y. Yamakawa, M. Hirayama, R. Kanno, M. Yonemura, T. Kamiyama, Y. Kato, S. Hama, K. Kawamoto, *Nat. Mater.* **2011**, *10*, 682–686.
[47] J. M. Doux, H. Nguyen, D. H. Tan, A. Banerjee, X. Wang, E. A. Wu, C. Jo, H. Yang, Y. S. Meng, *Adv. Energy Mater.* **2020**, *10*, 1903253.

Manuscript received: December 7, 2022
Accepted manuscript online: January 16, 2023
Version of record online: February 23, 2023